

ARTICLE OPEN



Solution processed low power organic field-effect transistor bio-chemical sensor of high transconductance efficiency

Wei Tang¹, Ying Fu², Yukun Huang¹, Yuanzhe Li², Yawen Song¹, Xin Xi¹, Yude Yu³, Yuezeng Su¹, Feng Yan^{1,2}✉ and Xiaojun Guo¹✉

Developing organic field-effect transistor (OFET) biosensors for customizable detection of biomarkers for many diseases would provide a low-cost and convenient tool for both biological studies and clinical diagnosis. In this work, design principles of the OFET transducer for biosensors were derived to relate the signal-to-noise ratio (*SNR*) to the device-performance parameters. Steep subthreshold swing (*SS*), proper threshold voltage (V_{th}), good-enough bias-stress stability, and mechanical durability are shown to be the key prerequisites for realizing OFET bio-sensors of high transconductance efficiency (g_m/I_D) for large *SNR*. Combining a low trap-density channel and a high-*k*/low-*k* gate dielectric layer, low-temperature (<100 °C) solution-processed flexible OFETs can meet the performance requirements to maximize the g_m/I_D . An extended gate-structure OFET biosensor was further implemented for label-free detection of miR-21, achieving a detection limit below 10 pM with high selectivity at a low operation voltage (<1 V).

npj Flexible Electronics (2022)6:18; <https://doi.org/10.1038/s41528-022-00149-9>

INTRODUCTION

There are rapidly growing demands for ubiquitous perception of various biomarkers (ions or biomolecules) in blood, body fluids, secretions, excrement, and tissue cells of human for personalized medical diagnosis and healthcare^{1,2}. To realize that, the biosensing devices need to be highly customizable to meet diverse system requirements in terms of biocompatibility, cost, and form factor (compact, thin, flexible, or comfortable), while producing output signal of high-enough signal-to-noise ratio (*SNR*) under strict power constraint. The most affordable and convenient way would be based on electrical measurements, which avoid using additional bulky, power-hungry, and expensive optical components. Transducers made by integration of the sensor interface with a field-effect transistor (FET) have been widely studied, since the FET can convert the sensed signal into an amplified output signal for potentially large *SNR*³. In addition, with FET switches, multiplexed detection in a single reaction is convenient to be implemented for high-throughput and multi-analyte analysis. The organic FET (OFET), composed of organic semiconductors (OSCs) and polymer dielectric layers, shows several competitive advantages over inorganic counterparts for such biosensing applications^{4,5}. The use of solution-printing processes and versatile structures might facilitate integration of various sensing interfaces or probes at the device level in great freedom⁶. With low processing temperature and superior intrinsic mechanical flexibility of the full organic stacks, truly flexible sensor electronics can be fabricated using common low Young's modulus thin plastic foils with much less stress-management efforts⁷. In the past, OFETs have been studied for detecting various biomolecules, including enzyme, DNA, and protein^{8–11}. As a popularly used approach, probes are immobilized on the gate or its extended part to capture the target molecules. Once the molecules are being captured, the resulted potential change at the gate is recorded or converted to output-current change through the OFET for further processing. These work well proved that the capability of OFETs to be designed for various biosensing functions through material-

and device-structure engineering. However, many of the devices required vacuum processes and inorganic dielectric layers, which would sacrifice the technical competence of the OFET.

Although solution-based processes at low temperature might offer attractive features for high customizability at low cost, they suffer difficulties in fine control of layer thickness, especially for very-thin films, and formation of high-quality semiconductor/dielectric films and interfaces. With such constraints, the achievable device performance is severely limited. In the past, there have been significant efforts on improving the carrier mobility in the OSC channels through material molecule design and crystallization-controlled processing methods^{12,13}. However, for biochemical sensors to detect very low concentration of analyte in various portable, wearable, or implantable scenarios, large *SNR* with low operating voltage and power would be a prerequisite^{14–16}. However, there is lack of studies on optimal design of the OFET for such figure of merits considering the interplay between device structures and material stacks under processing constraints.

This work derives the OFET-design principles for biochemical sensor transducers of large transconductance efficiency (g_m/I_D) for large *SNR* with low operation voltage. Steep subthreshold swing (*SS*), proper threshold voltage (V_{th}), and operational stability are shown to be the key parameters to determine the optimal performance. Based on the design principles, low-voltage OFETs are then fabricated on plastic substrate in low-temperature solution processes to obtain the required performance, through formation of a low trap-state density channel interface on high-*k*/low-*k* bilayer-structure gate insulator. To verify its transduction performance, a plastic sensor tag is implemented through encapsulating the OFET with a sensing electrode and a reference electrode for miRNA detection. miRNAs are key biomarkers for many diseases, and label-free miRNA detection in electrochemical ways would provide low-cost and convenient tools for both biological fundamental studies and clinical diagnosis¹⁷. However, miRNAs are of low charge level due to their short intrinsic molecule length, and thus challenging to be detected at very low

¹School of Electronic Information and Electrical Engineering, Shanghai Jiao Tong University, Shanghai 200240, China. ²Department of Applied Physics, The Hong Kong Polytechnic University, Hong Kong, China. ³State Key Laboratory of Integrated Optoelectronics, Institute of Semiconductors, Chinese Academy of Sciences, Beijing 100083, China. ✉email: apafyan@polyu.edu.hk; x.guo@sjtu.edu.cn

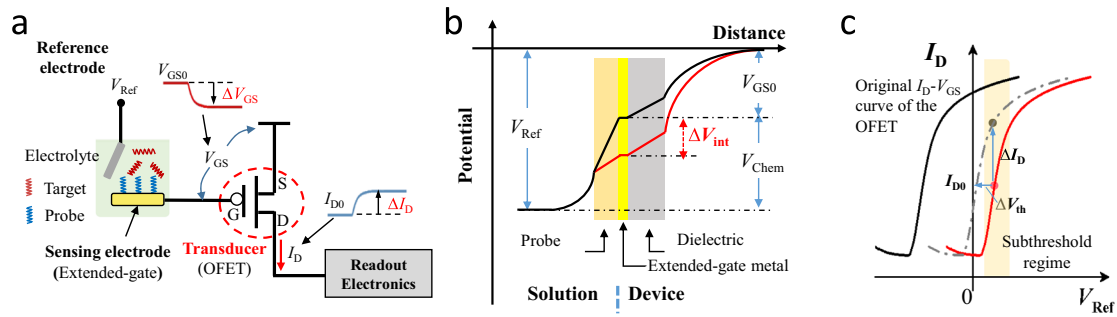


Fig. 1 Illustration of an OFET-based biochemical sensor. **a** Schematic of the biosensor design for analyte detection in electrolyte solution. The biosensor consists of an OFET transducer and an extended-gate sensing electrode immobilized with probes. V_{Ref} is the bias voltage at the reference electrode (Ag/AgCl). V_{GS} is the resulted gate-to-source voltage on the OFET. I_{D} is the drain current to be measured by the subsequent readout electronic system. **b** Diagram for potential over a simplified electrochemical cell model with an extended-gate metal as the interfacial material for sensing. The charged molecules captured onto this surface create a potential shift (ΔV_{int}) at the solution/metal interface and thus equal ΔV_{GS} seen from the OFET. **c** Illustration of the transfer-curve shift from the $I_{\text{D}}-V_{\text{GS}}$ curve of the OFET to the $I_{\text{D}}-V_{\text{Ref}}$ curve when the OFET sensor is tested in solution by sweeping V_{Ref} , and the induced significant output-current change from the background level (ΔI_{D}) in the subthreshold regime even at a small threshold-voltage shift (ΔV_{th}).

concentration. This work demonstrates the feasibility of using the OFET for miRNA sensing. With the optimal device performance, the sensor exhibits a 20% relative output-signal change over the background upon detection of miR-21 (a miRNA biomarker for breast cancer) at 10 pM under an operation voltage less than one volt.

RESULTS AND DISCUSSION

Design principles

Figure 1a illustrates the structure of an OFET-based biochemical sensor, consisting of an OFET transducer with an extended-gate sensing electrode (SE), and a reference electrode (RE). The probe-immobilized SE is to capture analyte targets in solution through specific target/probe combination. For measurement, a constant voltage bias (V_{Ref}) is applied to the RE, inducing an initial potential at the OFET gate (V_{GS0}) through the solution and in turn a channel current in the OFET (I_{D0}). As depicted in Fig. 1b, V_{GS0} can be expressed as:

$$V_{\text{GS0}} = V_{\text{Ref}} - V_{\text{Chem}} \quad (1)$$

where V_{Chem} is the voltage between the RE and the SE, and can be assumed to be a sum of a constant V_{Chem0} and an interfacial potential drop (V_{int0})¹⁸. The interfacial potential drop V_{int0} , arising from the electrode/electrolyte interfacial dipole, is modulated with the captured charged biomolecules and can be measured by using the open circuit potential method¹⁹. When the SE detects a certain concentration of analyte targets in the solution, the captured negatively (or positively) charged targets would induce a change of the interfacial potential drop (ΔV_{int}), and thus ΔV_{GS} . Correspondingly, an output-current change (ΔI_{D}) can be measured by the subsequent readout circuit for digitalization, as shown in Fig. 1a.

The detection limit of the whole system is determined by the signal-to-noise ratio (SNR) of the OFET transducer, which is given as^{16,20}

$$\text{SNR} = 10 \log \left(\frac{P_{\text{signal}}}{P_{\text{noise}}} \right) \quad (2)$$

where P_{signal} is the signal power and P_{noise} is the noise power. According to the aforementioned analysis, P_{signal} is contributed by ΔI_{D} upon detection of a certain concentration of analyte. For low-frequency biochemical sensing, P_{noise} is mainly dominated by $1/f$ noise and can be described as⁷

$$i_{1/f}^2 = K \frac{\beta}{f\alpha} \quad (3)$$

where I is the operation current, K is a process-dependent coefficient, f is the frequency, and α and β are noise parameters (with $\alpha = 1$ and $\beta = 2$ in theory in subthreshold regime). Correspondingly, the SNR for an OFET transducer operating in subthreshold regime at low frequency is deduced to be:

$$\text{SNR} = 10 \log \left(\frac{P_{\text{signal}}}{P_{\text{noise}}} \right) = 10 \log \left(\frac{\Delta I^2}{i_{1/f}^2} \right) \approx 10 \log \left(\frac{\Delta I^2}{\frac{f}{K} \left(\frac{\Delta I}{I} \right)^2} \right) \quad (4)$$

According to (4), the SNR depends on the relative current-output signal change over the background level ($\Delta I/I$). As a result, to improve the detection limit, it would be important to maximize $\Delta I_{\text{D}}/I_{\text{D0}}$ of the OFET transducer for a certain concentration of analytes. $\Delta I_{\text{D}}/I_{\text{D0}}$ can be described as

$$\frac{\Delta I_{\text{D}}}{I_{\text{D0}}} = \frac{g_{\text{m}} \Delta V_{\text{GS}}}{I_{\text{D0}}} = - \frac{g_{\text{m}}}{I_{\text{D0}}} \cdot \Delta V_{\text{int}} = - \left(\frac{\ln 10}{SS} \right) \cdot \Delta V_{\text{int}} \quad (5)$$

where g_{m} is transconductance and SS is the subthreshold swing. Therefore, to maximize $\Delta I_{\text{D}}/I_{\text{D0}}$, enlarging the transconductance efficiency ($g_{\text{m}}/I_{\text{D0}}$) is as important as achieving effective immobilization of specific targets on the gate electrode (increasing ΔV_{int}). In other words, $g_{\text{m}}/I_{\text{D0}}$ is an important figure-of-merit to benchmark the sensing capability of extended-gate OFET sensors. Since the maximum of $g_{\text{m}}/I_{\text{D0}}$ occurs in the subthreshold regime, and is proportional to the inverse of SS ⁷, steep SS would thus be required to design OFET transducers of high $g_{\text{m}}/I_{\text{D}}$ for large SNR.

As illustrated in Fig. 1c, when the OFET is operated in the sensor system, the obtained transfer curve by sweeping V_{Ref} would have a shift compared with the original $I_{\text{D}}-V_{\text{GS}}$ curve of the OFET. Such a shift is due to the presence of an interfacial potential between the surface of the gate electrode and the aqueous solution²¹. To enable operation of the OFET in the subthreshold regime with a small V_{Ref} , a proper near-zero threshold voltage (V_{th}) is also required. Operational stability is another concern to be considered, since a certain waiting time (i.e., tens of minutes) is often required for interaction between the probes and the target biomolecules²². As illustrated in Fig. 1c, when the OFET is biased in the subthreshold regime, even a slight V_{th} shift would induce significant output-current change (ΔI_{D}), causing false-positive or false-negative results. Similar to the electrical bias stress, since the flexible device is inevitably subject to some bending state, attention should also be paid to the mechanical durability during bending stress.

According to the above analysis, it is concluded that steep SS , proper threshold voltage, and operational stability under electrical bias and mechanical stress are key prerequisites for designing low-power OFET biochemical sensor transducers of large SNR.

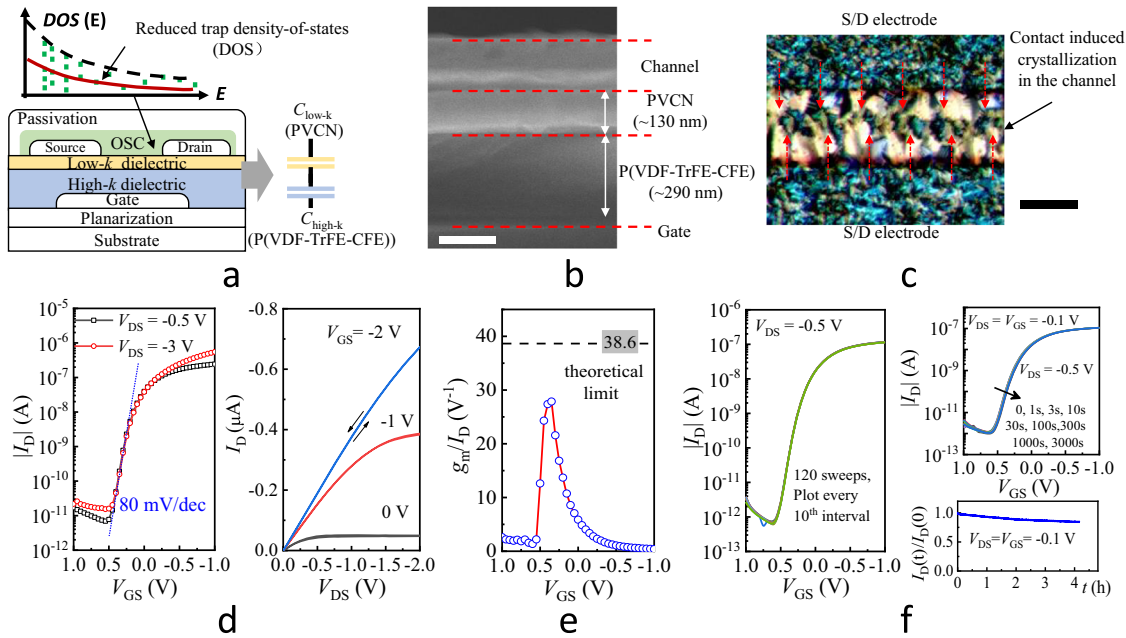


Fig. 2 Microscopic and electrical characterization of OFET. **a** Schematic of the OFET in a bottom-gate bottom-contact structure fabricated on a polyethylene naphthalate (PEN) substrate combining low trap density-of-state (DOS) channel and high- k /low- k gate dielectric layer. **b** Cross-sectional scanning electron microscopy (SEM) image showing the material stack of the OFET. The scale bar is 200 nm. **c** Polarized optical micrograph showing contact-induced crystallization along the channel with the perfluorobenzenethiol-modified silver source/drain electrodes. The scale bar is 50 μm . **d** Measured typical transfer (I_D - V_{GS}) and output (I_D - V_{DS}) characteristics with well-behaved field-effect transistor behaviors and a steep subthreshold swing of about 80 $\text{mV}/\text{dec}^{-1}$ ($W/L = 2000 \mu\text{m}/70 \mu\text{m}$). **e** The extracted transconductance efficiency (g_m/I_D) as a function of the gate-to-source voltage (V_{GS}) with the maximum value of 28.8 V^{-1} exceeding those of previously reported extended-gate OFET biosensors. **f** Left: the measured I_D - V_{GS} curves at each 10^{th} interval under continuously sweeping V_{GS} from OFF to ON for 120 times. Right: the measured I_D - V_{GS} curves under continuous bias stress ($V_{GS} = V_{DS} = -0.1 \text{ V}$) with the measured normalized drain current over the original value ($I_D(t)/I_D(0)$) for 4 h.

Device fabrication and characterizations

To meet the requirements as discussed above, an OFET design combining a low trap-state density channel and a high- k /low- k gate dielectric layer is implemented, to achieve steep SS and near-zero V_{th} , while using a thick-enough dielectric layer for large-area solution processability. As shown in Fig. 2a, the devices were fabricated in a bottom-gate bottom-contact structure on a polyethylene naphthalate (PEN) plastic substrate. The gate and source/drain electrodes were formed by thermal evaporation of silver (Ag) through shadow masks. The gate dielectric was composed of a low- k poly(vinyl cinnamate) (PVCN) layer and a high- k poly(vinylidene fluoride-trifluoroethylene-chlorofluoroethylene) (P(VDF-TrFE-CFE)) layer with total thickness of about 420 nm, as shown by the cross-sectional scanning electron microscopy (SEM) image (Fig. 2b). Both layers were deposited by spin-coating processes followed by low-temperature annealing. The surfaces of the source/drain electrodes were treated by perfluorobenzenethiol (PFBT) before deposition of the organic semiconductor (OSC) layer. The OSC layer was deposited using a blade-coating process from a blended solution of 6,13-bis(triisopropylsilyl)ethynyl-pentacene (TIPS-pentacene) and polystyrene (PS)²³. Well-crystalline structure channels can be formed as shown in Fig. 2c to obtain a low-trap OSC/dielectric interface for steep SS at small-gate dielectric capacitance ($20.1 \text{ nF}/\text{cm}^2$). A CYTOP passivation layer was finally deposited by drop-casting to protect the channel from the air ambient. Details of the fabrication processes are described in “METHODS”. The maximum processing temperature is kept below 100 $^\circ\text{C}$.

The measured representative transfer (I_D - V_{GS}) and output (I_D - V_{DS}) characteristics of the sealed OFET are shown in Fig. 2d, presenting well-behaved FET behaviors with a steep SS of about 80 $\text{mV}/\text{dec}^{-1}$, a nearly zero V_{th} (0.3 V), and an ON/OFF ratio larger than 10^5 . From the SS value, the effective subgap trap density is

estimated to be $4.3 \times 10^{10} \text{ eV}^{-1} \cdot \text{cm}^{-2}$, similar to previous work using a single low- k gate dielectric layer²⁴ and also superior to those used in extended-gate OFET biosensors (Supplementary Table 1). The measured g_m/I_D versus V_{GS} is plotted in Fig. 2e, with its maximum value of 28.8 V^{-1} exceeding those of previously reported extended-gate OFET biosensors (Supplementary Table 1). The maximum g_m/I_D occurring at $V_{GS} = 0.35 \text{ V}$ enables the OFET to be used in the sensor system as depicted in Fig. 1a for biomolecule detection of high sensitivity and low detection limit at low $V_{\text{Ref}} (< 1 \text{ V})$.

The operational stabilities under continuous switching and constant bias stress were characterized and shown in Fig. 2f. The device exhibits nearly identical transfer characteristics after sweeping between OFF and ON for 120 times. With a bias stress at a V_{GS} near threshold voltage for 3000 s, there is negligible V_{th} shift (less than 0.01 V). The relative current change ($\Delta I_D(t)/I_D(0)$) is less than 15% after constant bias stress for more than 4 hours. Such a device design owns low-trap OSC/dielectric interface, and is operated with low charge density and weak perpendicular electrical field at low voltage attributed to a thick-gate dielectric layer²⁵. Compared with the implemented low-voltage device using ultrathin dielectric of high capacitance, these factors reduce the probability of charge trapping under bias stress, and thus enable the device to achieve high operational stabilities. Large g_m/I_D , proper V_{th} , and high operational stability make the device a promising transducer for biomolecule detection.

Evaluation of mechanical stability

The mechanical stability of the flexible OFET device encapsulated by CYTOP was evaluated by measuring its electrical characteristics with changing bending angles. Figure 3a shows the measurement system for assessing the stability of the OFET device under bending states. The investigated bending angle (θ)

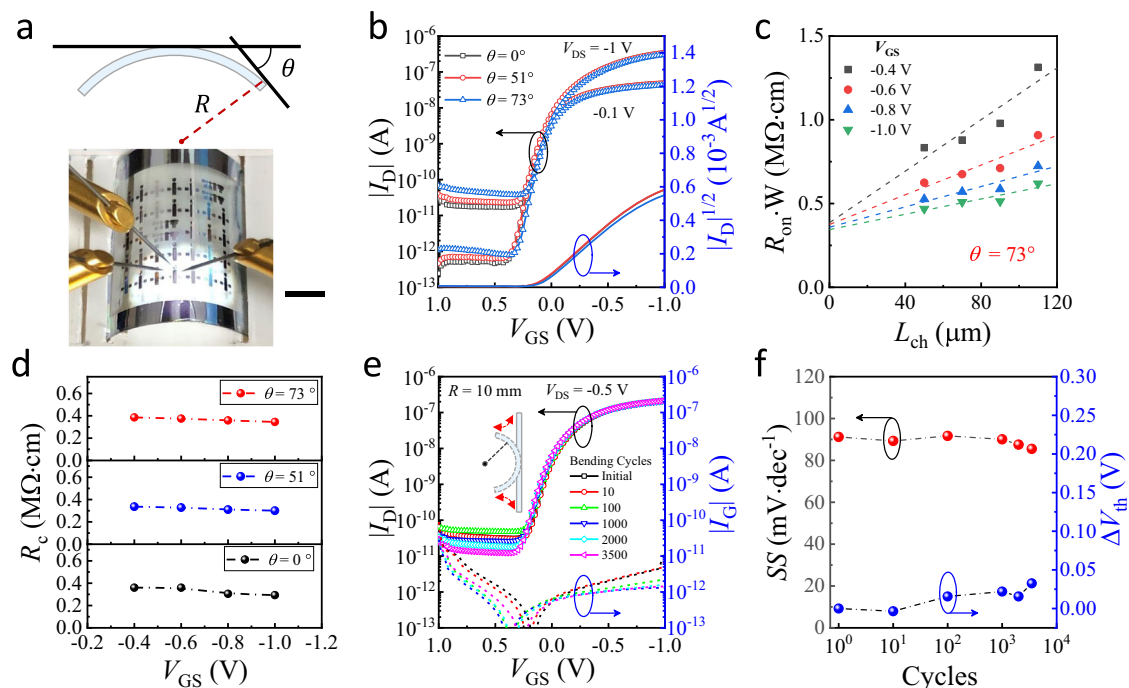


Fig. 3 Flexible OFET subjected to bending test. **a** Photoimage of a measured device under bending test with the schematic of bending angle (θ) and radius (R). The scale bar is 5 mm. **b** Transfer characteristics of OFETs ($W/L = 1500\ \mu\text{m}/90\ \mu\text{m}$) at different bending angles. **c** The measured channel-width-normalized total on-resistance ($R_{\text{ON}} \cdot W$) for flexible OFETs of different channel lengths (L_{ch}) bent at 73° . **d** The extracted contact resistance (R_c) at different V_{GS} for different bending angles based on the transmission-line method (TLM). **e** Transfer characteristics after different bending cycles (bending radius = 10 mm) and **(f)** the resulted change in subthreshold swing (SS) and threshold voltage (ΔV_{th}).

and radius (R) for the OFET under bending test are illustrated in Supplementary Fig. 1. Figure 3b shows the transfer characteristics of the OFET device before and after undergoing bending at various angles, presenting negligible degradation in the subthreshold characteristics even at a large bending angle of about 73° . The corresponding output characteristics (Supplementary Fig. 2) also show no apparent change after bending by about 51° , while only a slight degradation of on-current was observed after aggressively bending by about 73° . In this regard, the contact resistance (R_c) during the bending test was further estimated by using a transfer-line method (TLM). It is realized by taking the total normalized on-resistance ($R_{\text{ON}} \cdot W$) from the output characteristics of OFET devices with various channel lengths in the linear regime and then extrapolating the linear fit to a channel length of zero to obtain R_c . As shown in Supplementary Fig. 3, the bent OFETs with channel length ranging from 50 to $110\ \mu\text{m}$ present well-behaved output performance with a clear saturation of the drain current beyond the pinch-off point. Accordingly, the corresponding width-normalized $R_{\text{ON}} \cdot W$ can be calculated and plotted as a function of channel length for OFET under different bending conditions (Supplementary Fig. 4). As shown in Fig. 3c, the R_c extracted by TLM at the most significant bending angle of 73° is approximately $0.3 \sim 0.38\ \text{M}\Omega \cdot \text{cm}$. Although such R_c is slightly dependent on the gate bias voltage, it remains nearly unchanged during the measured bending states (Fig. 3d). Electrical measurements of the flexible device were further performed under bending stress. For this purpose, a stressing cycle was applied to the device by repeatedly bending it to radius = 10 mm and immediately releasing it to its initial state at a rate of 12 times per minute. Figure 3e shows that the flexible OFET device maintained well-functional transfer characteristics during the bending stress. Even after 3500 complete cycles, the change in subthreshold swing was not exceeding $5\ \text{mV} \cdot \text{dec}^{-1}$, while threshold voltage shift was less than $0.03\ \text{V}$ (Fig. 3f), revealing negligible change in subthreshold performance during

the performed bending stress. These results illustrate that the developed low-voltage OFET can sustain the inevitable bending during usage and maintain its electrical performance for proper signal transducing.

Probe immobilization and hybridization

To verify the device concept of the designed OFET transducer for biosensing, this work takes miR-21 detection as an example, which is one of the potential candidate biomarkers for primary breast cancer²⁶. The scheme for immobilizing probes on the extended-gate SE is depicted in Fig. 4a. A thiolated single-stranded DNA (ssDNA) probe was designed to match the miR-21 for specific detection. Based on the well-established thiol-gold chemistry, the ssDNA probes and the 6-mercapto-1-hexanol (MCH) were able to self-assemble onto the gold electrode surface efficiently via a strong SH-gold binding. The ssDNA probes work as the receptor for capturing miRNA targets, while the MCH, as a blocking layer, reduces miRNA-gold interaction and thus improves hybridization discrimination^{27,28}. As a result, the miR-21 targets were selectively captured on the extended-gate SE through DNA/miRNA hybridization according to the law of Watson-Crick base-pairing²⁹.

To verify the hybridization-reaction procedure, miR-21 was labeled with fluorescent dyes (FAM) for fluorescence measurement. As shown in Fig. 4b, the ssDNA-immobilized gold incubated to the 1X phosphate-buffered saline (PBS 1X) solution shows no fluorescence. After incubation of the electrode surface to the FAM-labeled miR-21 solution, there is weak fluorescence at a miR-21 concentration of $10\ \text{pM}$, while obvious fluorescence occurring at a concentration of $1\ \text{nM}$. With increase of the concentration to $100\ \mu\text{M}$, the signal becomes strong. The results prove the hybridization reaction between the miR-21 targets and the ssDNA probes.

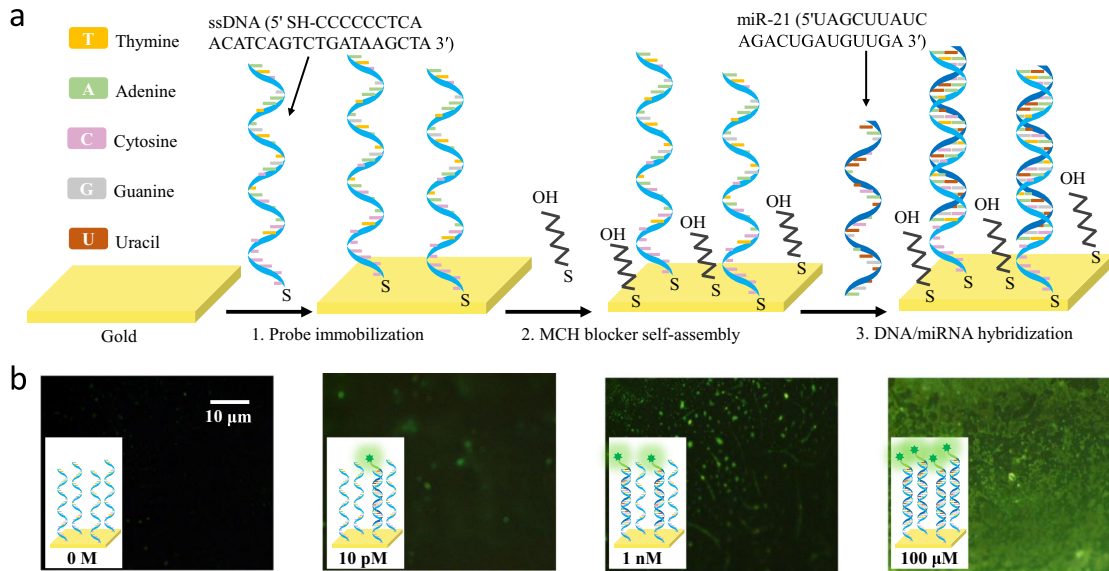


Fig. 4 Fluorescence image of extended-gate sensing electrode. **a** Illustration of the scheme for immobilizing the designed ssDNA probes on the extended-gate sensitive electrode for specific detection of miR-21 through DNA/miRNA hybridization. **b** Fluorescence images for ssDNA-immobilized gold incubated to the PBS 1X solution, and the solutions containing fluorescent dyes labeled miR-21 of different concentrations: 10 pM, 1 nM and 100 μ M, respectively.

Implementation of miRNA sensor

The individual OFET was cut from the fabricated large area sample, and then encapsulated onto a carrier PEN substrate with the extended-gate SE and the Ag/AgCl RE to complete a sensor tag for use as shown in Fig. 5a. The encapsulation processes are described in details in "METHODS". After the extended-gate SE and the RE being placed in the PBS 1X solution, the I_D - V_{Ref} curve was measured by sweeping V_{Ref} at a $V_{DS} = -0.5$ V, presenting an obvious shift to the negative direction compared with the I_D - V_{GS} curve of the pristine OFET, as seen in Fig. 5b. After immobilization of ssDNA probes onto the extended-gate SE, there is a small shift backward due to the negatively charged probes. As a result, with a proper V_{th} , the OFET transducer was able to be biased in the subthreshold regime for large g_m/I_D at a low V_{Ref} (-0.1 V). Figure 5c shows the measured I_D - V_{Ref} curves using the same sensor when the concentration of miR-21 targets varies from 0 to 1 μ M. V_{th} values were extracted from the I_D - V_{Ref} curves at a drain current of 1 nA. The measured V_{th} shift (ΔV_{th}) at various concentrations of miR-21, calculated by using the V_{th} value at 0 M of miR-21 as blank ($\Delta V_{th} = V_{th}^{miRNA} - V_{th}^{Blank}$), is shown in Fig. 5d. The solution containing a 3-base mismatch miRNA of a much higher concentration (100 μ M) was also tested for comparison. The results show that ΔV_{th} for the lowest measured miR-21 concentration (10 pM) is 16.9 ± 5 mV, much higher than the value (0.2 ± 5 mV) for 3-base mismatch miRNAs of high concentration (100 μ M), indicating high selectivity. Moreover, the limit of detection (LOD) was used to interpret the detectability of the sensor. It is defined as the concentration that leads to a sensor response equal to three times the standard deviation of the negative control sample ($\Delta V_{th}^{mean} \pm 3\sigma$), where ΔV_{th}^{mean} is the average response, and σ is the relative standard deviation³⁰. According to this definition, the LOD was estimated to be 4.5 pM by taking the response of 3-base mismatch miRNA as the negative control sample. Note that the response at 10 pM is beyond the LOD (Fig. 5d), verifying the OFET biosensor's high sensing capability at such a low concentration. The measured relative current change ($\Delta I_D/I_{D0}$) at $V_{Ref} = -0.1$ V for various miR-21 concentrations is shown in Fig. 5e. For a low concentration of 10 pM, $\Delta I_D/I_{D0}$ of 20% is able to be obtained for large-enough SNR to be processed by the subsequent readout electronics for digitalization. Therefore, the sensor is able to achieve a detection

limit below 10 pM to the target miRNAs with good selectivity at a low operation voltage (<1 V). The overall performance shows competence over that of the previous work based on a Si-FET in Table 1, in terms of the detection limit, the operation voltage, and the static power³¹.

In summary, the derived design principles of the OFET transducer for biosensors build relationships between the SNR and the key OFET-performance parameters, including g_m/I_D , SS, V_{th} and bias-stress stability. Combining a low trap-state density channel and high- k /low- k structure gate dielectric, OFETs fabricated on PEN substrate with low temperature solution-based processes can meet the optimal design requirements, exhibiting steep SS, near-zero V_{th} , and good-enough bias-stress stability and mechanical durability. Extended-gate structure OFET biosensors were further constructed for label-free detection of miR-21, a potential biomarker for primary breast cancer. The results demonstrate that the sensor can achieve a detection limit below 10 pM to the target miRNAs with good selectivity at a low operation voltage (<1 V). The overall performance is competitive over that of the previous work based on the Si-FET, in terms of the detection limit, the operation voltage and the static power. This work would pave the way to developing low-cost and convenient biosensors based on OFETs to have large SNR for customizable detection of disease biomarkers in both biological studies and clinical diagnosis.

METHODS

Materials and reagents

In all, 125- μ m-thick polyethylene naphthalate (PEN) plastic films (Teonex Q65HA) were purchased from DuPont Teijin Films. Poly (vinyl cinnamate) (PVCN, $M_w = 40$ kDa), polystyrene (PS, $M_w = 524$ kDa), perfluorobenzenethiol (PFBT), and 6-mercapto-1-hexanol (MCH) were purchased from Sigma-Aldrich. Poly(vinylidene fluoride-trifluoroethylene-chlorofluoroethylene) (56/36.5/7.5 mol%) terpolymer (P(VDF-TrFE-CFE)) was synthesized by the suspension-polymerization process³². 6,13-bis(triisopropylsilylethynyl)-pentacene (TIPS-pentacene) (FN4023) was provided by Merck Chemicals Ltd. CYTOP (CTL-809M) was obtained from Asahi Glass. Silver (Ag) pastes were obtained from Hisense Electronics, Kunshan, China. Silicone sealant was purchased from Shanghai Qianru Building Materials. Phosphate-buffered saline (PBS 1X, pH = 7.2) solution was obtained from Thermo Fisher Scientific. The sequences of probe single-stranded DNA (5'-SH-CCCCCTCAACATCAGTCTGATAAGCTA-3'),

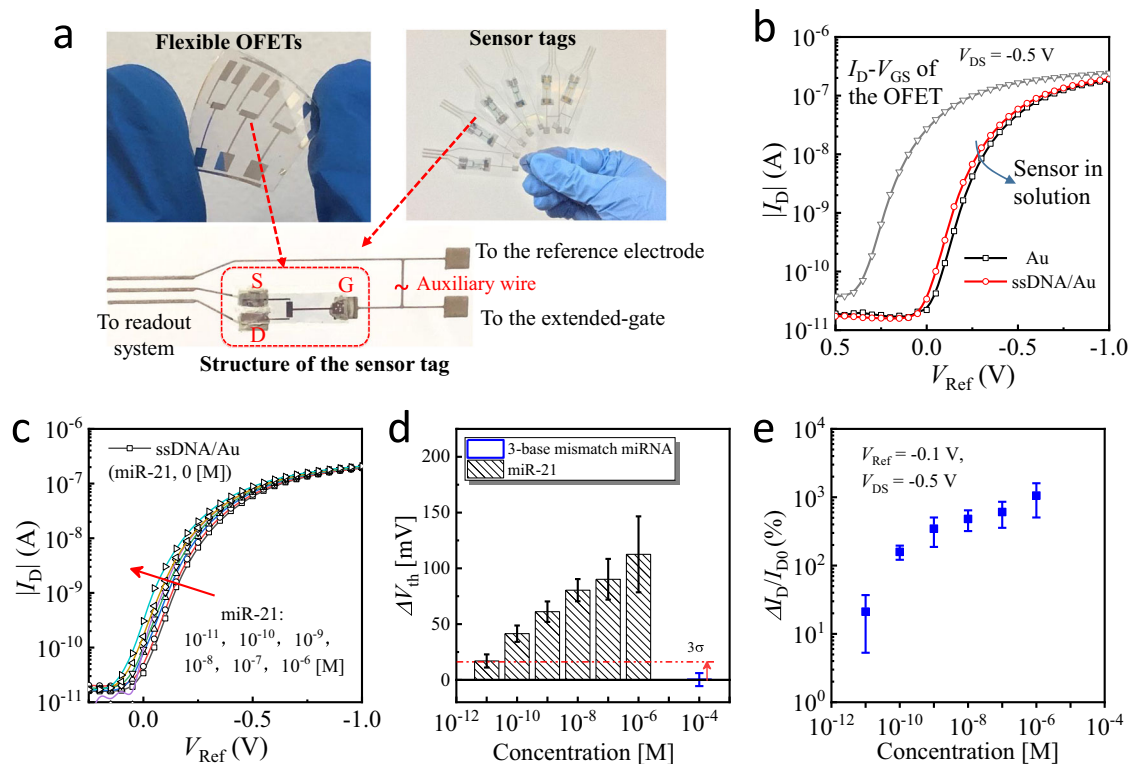


Fig. 5 Performance of low-voltage OFET miRNA sensor. **a** Photo images of the fabricated OFETs on PEN substrate, and the sensor tags consisting of an encapsulated OFET and contacts for extended-gate sensing electrode and reference electrode. **b** Measured I_D - V_{Ref} curve by sweeping V_{Ref} after the sensor being placed in the electrolyte solution, presenting an obvious shift to the negative direction compared with the I_D - V_{GS} curve of the pristine OFET. After immobilization of ssDNA probes onto the sensing electrode, there is a small shift backward due to the negatively charged probes. **c** Measured I_D - V_{Ref} curves for the concentration of miR-21 targets varying from 0 to $1 \mu\text{M}$. **d** Extracted V_{th} shift (ΔV_{th}) of the curves at various concentrations of miR-21 with the test results for the 3-base mismatch miRNA as the background level. The dashed lines indicate the limit of detection (LOD) obtained from three-times the standard-measurement error bar of the blank noise. Error bars indicate standard deviations. **e** The measured relative current change from the background level ($\Delta I_D/I_{D0}$) at $V_{\text{Ref}} = -0.1 \text{ V}$ for various miR-21 concentrations. Error bars indicate standard deviations.

Transistor	Si-FET ^[31]	OFET
Detection limit	1 nM	<10 pM
Operation voltage	1.9 V	<1 V
Static Power	~40 μW	<5 nW
$\Delta I/I_0$ at low concentration	37.5% at 1 nM	20% at 10 pM

fully complementary target miR-21 (5'-UAGCUUAUCAGACUGAUGUUGA-3'), noncomplementary 3-base mismatch miRNA (5'-UAGCCUAUCAACUGAUGAUGA-3'), and fluorescence-dyed miR-21 (5'-FAM-UAGCUUAUCAGACUGAUGUUGA-3') used in this study were synthesized by Sangon Biotech (Shanghai) Co. Ltd., China.

Device fabrication

OFET devices in a bottom-gate bottom-contact structure were fabricated on a plastic PEN foil laminated on a glass carrier. PVCN was dissolved in chlorobenzene with a concentration of 10 mg/ml and spin-coated at 3000 rpm onto the substrate as a planarization layer, followed by UV cross-linking (UV Curer KW-4AC, CHEMAT) for 20 min and then heating at 100°C for 1 h. Next, 40 nm-thick silver (Ag) gate electrodes were deposited by thermal evaporation using a stainless-steel mask. Then, a high- k P (VDF-TrFE-CFE) (dissolved in methyl ethyl ketone, 40 mg/ml) and a low- k PVCN (dissolved in chlorobenzene, 10 mg/ml) were subsequently spin-coated to form a thick bilayer-gate dielectric. Ag source/drain (S/D) electrodes were obtained using the same processes as that for formation

of the gate electrodes, defining a channel width of $2000 \mu\text{m}$ and a channel length of $70 \mu\text{m}$, respectively. Devices with the same channel width ($1500 \mu\text{m}$) and a series of channel lengths (50, 70, 90, and $110 \mu\text{m}$) were also used to evaluate the mechanical stability. Before the deposition of the semiconductor layer, the sample was immersed into a PFBT solution (5 mM in isopropanol) for 15 min to form self-assembled monolayers on the S/D electrodes. After this treatment, it was carefully rinsed with isopropanol and blown by dry N_2 gas, followed by annealing at 100°C on a hot plate for 1 min. The semiconductor/polymer-blended solution was prepared by mixing TIPS-pentacene and PS solutions (dissolved in chlorobenzene, $10 \text{ mg}\cdot\text{mL}^{-1}$) in 3:1 ratio by volume. The semiconducting film was formed using a soft-contact coating approach with a rotatable steel sheet as the meniscus guide at coating speed of 20 mm/s , followed by annealing at 100°C for 30 min²³. Finally, CYTOP solution ($10 \mu\text{L}$) was drop-cast to passivate the channel and annealed at 80°C for 30 min.

Sensor-tag encapsulation

After completing the preparation of OFET device, its supporting PEN foil was carefully peeled off from the glass carrier. Subsequently, individual CYTOP-passivated OFET was cut from it to mount onto another holding PEN substrate with prefabricated screen-printed silver interconnects and pads. A bonding process was developed by flipping over the OFET device and attaching to the substrate using silver paste, followed by annealing at 80°C for 10 min. Finally, a silicone sealant was dispensed with a dispenser robot to seal the device.

Sensing-electrode preparation

Extended-gate sensing electrode consisting of chromium (10 nm) and gold (100 nm) was deposited using magnetron sputtering, which was further encapsulated with silicone sealant to define a sensing area of 9 mm^2 . Prior to immobilization of probes, the electrode surface was cleaned by O_2

plasma for 10 min. Then, 10 μL of 5'-SH-modified capture ssDNA solution (10^{-4} M , dissolved in PBS 1X) was added onto the gold electrode and incubated at 4°C in humid condition overnight, followed by rinsing thoroughly with PBS 1X solution. After immobilization of probes, the electrode was posttreated with 10 μL of MCH aqueous solution (1 mM) for 1 h to remove nonspecifically bound oligonucleotides and block extractive gold surface, followed by rinsing with PBS 1X solution. The obtained sensing electrodes were used immediately to subject to 10 μL of fully complementary targets (miR-21 or FAM-dyed miR-21) and noncomplementary targets (3-base mismatch miRNA) diluted to desired concentrations in PBS 1X solutions for hybridization, respectively, followed by rinsing with PBS 1X solution carefully.

Characterization and measurement

The polarized optical micrograph for TIPS-pentacene crystalline was taken with a microscope (XPF-300C, Caikon). The fluorescence images were obtained from inverted fluorescence microscopy (IX71, Olympus Life Science). The cross-sectional scanning electron microscopy (SEM) image was obtained on a Zeiss Ultra Plus Field Emission Scanning Electron Microscope at an electric voltage of 5 kV. The cyclic bending test of the flexible OFET was performed on a stretching machine at bending radius of 10 mm with a speed of 5 s/cycle. The sensor tag was connected to the extended-gate sensing electrodes and reference electrode (Ag/AgCl) via copper wires. The electrical characterizations of the OFETs and biosensors were performed using a semiconductor parameter analyzer (Keithley 4200 system). All measurements were carried out at room temperature in ambient air.

DATA AVAILABILITY

The data that support the findings of this study are available from the corresponding author upon reasonable request.

Received: 18 April 2021; Accepted: 10 February 2022;

Published online: 18 March 2022

REFERENCES

- Sakata, T. Biologically coupled gate field-effect transistors meet in vitro diagnostics. *ACS Omega* **4**, 11852–11862 (2019).
- Lee, M. Y., Lee, H. R., Park, C. H., Han, S. G. & Oh, J. H. Organic transistor-based chemical sensors for wearable bioelectronics. *Acc. Chem. Res.* **51**, 2829–2838 (2018).
- Syu, Y.-C., Hsu, W.-E. & Lin, C.-T. Review-field-effect transistor biosensing: devices and clinical applications. *ECS J. Solid State Sci. Technol.* **7**, Q3196–Q3207 (2018).
- Zang, Y., Huang, D., Di, C. A. & Zhu, D. Device engineered organic transistors for flexible sensing applications. *Adv. Mater.* **28**, 4549–4555 (2016).
- Magliulo, M., Manoli, K., Macchia, E., Palazzo, G. & Torsi, L. Tailoring functional interlayers in organic field-effect transistor biosensors. *Adv. Mater.* **27**, 7528–7551 (2015).
- Khan, H. U. et al. In situ, label-free DNA detection using organic transistor sensors. *Adv. Mater.* **22**, 4452–4456 (2010).
- Jiang, C., Cheng, X. & Nathan, A. Flexible ultralow-power sensor interfaces for E-skin. *Proc. IEEE* **107**, 2084–2105 (2019).
- Lai, S., Barbaro, M. & Bonfiglio, A. Tailoring the sensing performances of an OFET-based biosensor. *Sens. Actuators B Chem.* **233**, 314–319 (2016).
- Song, J. et al. Influence of bioreceptor layer structure on myelin basic protein detection using organic field effect transistor-based biosensors. *Adv. Funct. Mater.* **28**, 1802605 (2018).
- Minamiki, T. et al. Accurate and reproducible detection of proteins in water using an extended-gate type organic transistor biosensor. *Appl. Phys. Lett.* **104**, 243703 (2014).
- Minami, T. et al. Selective nitrate detection by an enzymatic sensor based on an extended-gate type organic field-effect transistor. *Biosens. Bioelectron.* **81**, 87–91 (2016).
- Wang, C., Dong, H., Jiang, L. & Hu, W. Organic semiconductor crystals. *Chem. Soc. Rev.* **47**, 422–500 (2018).
- Gu, X., Shaw, L., Gu, K., Toney, M. F. & Bao, Z. The meniscus-guided deposition of semiconducting polymers. *Nat. Commun.* **9**, 534 (2018).
- Moser, N., Rodriguez-Manzano, J., Lande, T. S. & Georgiou, P. A scalable ISFET sensing and memory array with sensor auto-calibration for on-chip real-time DNA detection. *IEEE Trans. Biomed. Circuits Syst.* **12**, 390–401 (2018).
- Douthwaite, M., Koutsos, E., Yates, D. C., Mitcheson, P. D. & Georgiou, P. A thermally powered ISFET array for on-body pH measurement. *IEEE Trans. Biomed. Circuits Syst.* **11**, 1324–1334 (2017).
- Rajan, N. K., Brower, K., Duan, X. & Reed, M. A. Limit of detection of field effect transistor biosensors: effects of surface modification and size dependence. *Appl. Phys. Lett.* **104**, 084106 (2014).
- Kilic, T., Erdem, A., Ozsoz, M. & Carrara, S. microRNA biosensors: Opportunities and challenges among conventional and commercially available techniques. *Biosens. Bioelectron.* **99**, 525–546 (2018).
- Kaisti, M. et al. Real-time wash-free detection of unlabeled PNA-DNA hybridization using discrete fet sensor. *Sci. Rep.* **7**, 15734 (2017).
- Thompson, M. et al. Label-free detection of nucleic acid and protein microarrays by scanning Kelvin nanoprobe. *Biosens. Bioelectron.* **20**, 1471–1481 (2005).
- Liao, W. et al. pH sensing and low-frequency noise characteristics of low temperature (400°C) p-channel SOI schottky ISFETs. *IEEE Electron Device Lett.* **38**, 1146–1149 (2017).
- Ishige, Y., Shimoda, M. & Kamahori, M. Immobilization of DNA probes onto gold surface and its application to fully electric detection of DNA hybridization using field-effect transistor fet sensor. *Jpn. J. Appl. Phys.* **45**, 3776–3783 (2006).
- Xu, S. et al. Real-time reliable determination of binding kinetics of DNA hybridization using a multi-channel graphene biosensor. *Nat. Commun.* **8**, 14902 (2017).
- Huang, Y. et al. Scalable processing of low voltage organic field effect transistors with a facile soft-contact coating approach. *IEEE Electron Device Lett.* **40**, 1945–1948 (2019).
- Tang, W., Feng, L., Yu, P., Zhao, J. & Guo, X. Highly efficient all-solution-processed low-voltage organic transistor with a micrometer-thick low- k polymer gate dielectric layer. *Adv. Electron. Mater.* **2**, 1500454 (2016).
- Lee, W. H., Choi, H. H., Kim, D. H. & Cho, K. 25th anniversary article: microstructure dependent bias stability of organic transistors. *Adv. Mater.* **26**, 1660–1680 (2014).
- Mittal, S., Kaur, H., Gautam, N. & Mantha, A. K. Biosensors for breast cancer diagnosis: a review of bioreceptors, biotransducers and signal amplification strategies. *Biosens. Bioelectron.* **88**, 217–231 (2017).
- Qian, S. et al. Boronic acid functionalized Au nanoparticles for selective microRNA signal amplification in fiber-optic surface plasmon resonance sensing system. *ACS Sens* **3**, 929–935 (2018).
- Yang, C.-T., Pourhassan-Moghaddam, M., Wu, L., Bai, P. & Thierry, B. Ultrasensitive detection of cancer prognostic miRNA biomarkers based on surface plasmon enhanced light scattering. *ACS Sens* **2**, 635–640 (2017).
- Dorvel, B. R. et al. Silicon nanowires with high- k hafnium oxide dielectrics for sensitive detection of small nucleic acid oligomers. *ACS Nano* **6**, 6150–6164 (2012).
- Lu, N. et al. CMOS-compatible silicon nanowire field-effect transistors for ultrasensitive and label-free microRNAs sensing. *Small* **10**, 2022–2028 (2014).
- Ganguli, A., Watanabe, Y., Hwang, M. T., Huang, J.-C. & Bashir, R. Robust label-free microRNA detection using one million ISFET array. *Biomed. Microdevices* **20**, 45 (2018).
- Li, J., Sun, Z. & Yan, F. Solution processable low-voltage organic thin film transistors with high- k relaxor ferroelectric polymer as gate insulator. *Adv. Mater.* **24**, 88–93 (2012).

ACKNOWLEDGEMENTS

This work was financially supported by the National Natural Science Foundation of China under Grant (61334008, 61804094, and 61974091), National Science Fund for Excellent Young Scholars under Grant 61922057, and the Research Grants Council (RGC) of Hong Kong, China (Project No. C5015-15G).

AUTHOR CONTRIBUTIONS

X.G., Y.Y., and F.Y. conceived the idea. W.T. and X.G. designed the experiments, analyzed the data, and wrote the paper. Y.H. fabricated organic field-effect transistor and participated in tag preparation. Y.F. and Y.L. carried out the biosensor preparation and characterizations. X.X. performed the SEM imaging. Y.S. and Y.S. helped to analyze the data and revise the paper. X.G. and F.Y. supervised the project. All authors discussed the results and contributed to the preparation of the paper. W.T. and Y.F. contributed equally to this work.

COMPETING INTERESTS

The authors declare no competing interests.

ADDITIONAL INFORMATION

Supplementary information The online version contains supplementary material available at <https://doi.org/10.1038/s41528-022-00149-9>.

Correspondence and requests for materials should be addressed to Feng Yan or Xiaojun Guo.

Reprints and permission information is available at <http://www.nature.com/reprints>

Publisher's note Springer Nature remains neutral with regard to jurisdictional claims in published maps and institutional affiliations.



Open Access This article is licensed under a Creative Commons Attribution 4.0 International License, which permits use, sharing, adaptation, distribution and reproduction in any medium or format, as long as you give appropriate credit to the original author(s) and the source, provide a link to the Creative Commons license, and indicate if changes were made. The images or other third party material in this article are included in the article's Creative Commons license, unless indicated otherwise in a credit line to the material. If material is not included in the article's Creative Commons license and your intended use is not permitted by statutory regulation or exceeds the permitted use, you will need to obtain permission directly from the copyright holder. To view a copy of this license, visit <http://creativecommons.org/licenses/by/4.0/>.

© The Author(s) 2022